Coversheet for “Investigating the Relationship Between Sea Surface Temperature and the Mechanical Efficiency of Tropical Cyclones”

Author 1: Laurel Régibeau-Rockett (regirock@stanford.edu, Stanford University)
Author 2: Olivier Pauluis (op13@nyu.edu, New York University)
Author 3: Morgan O’Neill (oneillm@stanford.edu, Stanford University)

This manuscript is under peer review at *Journal of Climate*. We have submitted this preprint manuscript to the EarthArXiv server.

Investigating the Relationship Between Sea Surface Temperature and the Mechanical Efficiency of Tropical Cyclones

Laurel Régibeau-Rockett, [a] Olivier M. Pauluis,[b] and Morgan E O'Neill[a]

[a] *Department of Earth System Science, Stanford University, Stanford, California, US*

[b] *Courant Institute for Applied Mathematics, New York University, New York, New York, US*

Corresponding author: Laurel Régibeau-Rockett, laurelregibeau@gmail.com

ABSTRACT: Previous studies have investigated how sea surface temperature (SST) affects the potential intensity of tropical cyclones (TCs). However, this is an upper bound only on the maximum near-surface azimuthal winds, and does not fully account for the effects of atmospheric moisture. Potential intensity might not vary in the same way as the total kinetic energy (W_{KE}) of a TC would with changing SST. W_{KE} is related, via the conceptualization of the TC as a heat engine, to TC mechanical efficiency. We investigate how TC mechanical efficiency varies with SST in a series of moist, axisymmetric, radiative-convective numerical experiments with constant SSTs ranging from 295K to 307.5K. We find a -2.1 %K^{-1} decrease in the mechanical efficiency with SST. While the increase in the net heat energy gained by the TC heat engine acts to increase W_{KE}, the mechanical efficiency still decreases with SST due to the effects of moisture on W_{KE} and on the total heat input to the TC. Moist convection in an unsaturated atmosphere is associated with substantial irreversible entropy production, which detracts from the energy that the TC can use to power its winds. The increasing moisture content in a warmer atmosphere predicted by Clausius-Clapeyron scaling leads this irreversibility to increase in an unsaturated atmosphere, presenting a larger penalty on W_{KE} and decreasing the mechanical efficiency. Our results highlight the importance of giving full consideration to the effects of moisture on the TC heat engine in studies of how climate affects TCs.

SIGNIFICANCE STATEMENT: The purpose of this study is to investigate how the "mechanical efficiency" of tropical cyclones varies with sea surface temperature. This matters because the conceptualization of the tropical cyclone as a heat engine implies that the kinetic energy of its wind field is generated at this efficiency. The mechanical efficiency may be affected by changes in climate. Our results demonstrate that the mechanical efficiency decreases at -2.1 $\%K^{-1}$ with sea surface temperature, and in particular highlight the important role of moisture in this result.

1. Introduction

Tropical cyclones (TCs) are often destructive and dangerous phenomena, frequently causing loss of life and extensive property damage (Zhang et al. 2009; Klotzbach et al. 2018). A common conceptual model of the TC in a steady state is that of the TC as a heat engine (Emanuel 1986; Bister and Emanuel 1998). In this framework, energy is injected into the TC via latent and sensible heat fluxes from the warm, moist ocean surface, and lost to the environment via radiative cooling, primarily in the upper troposphere at a comparatively cool effective temperature. As with the Carnot heat engine, this heat transport allows the TC heat engine to generate work that balances the action of dissipation in steady state (Emanuel 1986; Bister and Emanuel 1998). Yet, unlike a classical heat engine, the total heat input to the TC heat engine is the same as the total heat output in steady state, which implies that the TC heat engine cannot generate any useful work. This is not incompatible with the TC heat engine generating nonzero work, including the kinetic energy of its wind field, because this constraint only applies to useful work that is used and dissipated externally to the TC, as in the classical heat engine. However, in a steady-state TC all generated work is used and dissipated inside the system (Bister et al. 2011; Bister and Emanuel 1998). This modified heat engine framework has proved illuminating in studying the thermodynamics and energetics of TCs (Pauluis 2016; Pauluis and Zhang 2017; Fang et al. 2019; Wang and Lin 2021). A major departure from the Carnot engine conceptual model is the moisture-associated irreversibility inherent in a real TC, which reduces the kinetic energy work that the TC heat engine can produce compared to its upper bound. Nearly all of this irreversibility is associated with phase changes of water in an unsaturated moist atmosphere and frictional dissipation associated with precipitation (Pauluis et al. 2000; Pauluis and Held 2002a,b; Pauluis 2011; Pauluis and Zhang 2017; Wang and Lin 2021).

The mechanical efficiency of a TC (Pauluis and Zhang 2017; Fang et al. 2019) is a property of the TC heat engine, defined as the fraction of the total heat input that is available to drive the full 3D wind field, and may vary with climate change. Changes in the mechanical efficiency are set by the combined variability of several energetic terms that reflect the impact of the distributions of temperature and moist entropy in a TC on its energetics, the effects of irreversibility associated with moisture on the kinetic energy produced by the TC heat engine, and the total heat input to the TC heat engine. Although some studies have examined aspects of the variability of the TC mechanical efficiency and related factors (e.g. Pauluis 2016; Pauluis and Zhang 2017; Fang et al. 2019; Wang and Lin 2021), much about this remains poorly understood. In this paper, we investigate how and why sea surface temperatures (SSTs), which are expected to generally increase with climate change, affect the mechanical efficiency of mature TCs.

Hakim (2011) created the first phase plot of a TC in the classical temperature-entropy space of heat engine diagrams, using the mean trajectory of a series of air parcels released at the point of maximum wind of a simulated axisymmetric TC. More recently, Pauluis (2016) developed the Mean Air Flow as Lagrangian Dynamics Approximation (MAFALDA), using the modified isentropic averaging procedure developed by Mrowiec et al. (2016), which allows the comprehensive study of TC mechanical efficiency using a moist, irreversible heat engine framework.

The question of how energetic terms related to the mechanical efficiency are affected by SSTs has not been answered comprehensively for TCs. Such a study has been performed for the global atmosphere (LaLiberté et al. 2015; Lembo et al. 2019; Knietzsch et al. 2015; Held and Soden 2006; Pan et al. 2017; Lucarini et al. 2010a,b) and for local atmospheric convection (Romps 2008; Singh and O'Gorman 2016; Pauluis 2016). Khairoutdinov and Emanuel (2013) study how the kinetic energy per unit surface area of an individual TC's wind field varies across a series of "TC-world" experiments with different SSTs. Other aspects of the thermodynamic behavior of TCs, such as the variability of their total kinetic energy and mechanical efficiency as the TCs intensify, have been studied using MAFALDA (Fang et al. 2019; Mrowiec et al. 2016; Pauluis and Zhang 2017; O'Neill and Chavas 2020; Li et al. 2023). This approach involves constructing cyclic thermodynamic trajectories that are assumed to represent a set of mean air parcel trajectories in the TC (Pauluis 2016). These trajectories range from thermodynamically very efficient trajectories that pass through the TC's eyewall (similar to those in Hakim (2011)) to very inefficient trajectories, which represent convection that occurs beyond the eyewall in rainbands. Previous studies mainly focus on one or two thermodynamic trajectories in a TC to perform these calculations, typically the most thermodynamically efficient trajectory. Relatively little attention has been paid to the behavior of all trajectories. Wang and Lin (2021) quantified a TC mechanical efficiency that effectively accounts for all trajectories via an entropy budget, and derived a relationship between the mechanical efficiency, the degree of irreversibility, and the compactness of the TC, where the latter is the focus of their study. The authors briefly discussed how changes in SST might affect the upper limit of the mechanical efficiency, defined according to classical TC heat engine theory (Emanuel 1986; Bister and Emanuel 1998). A mechanical efficiency effectively accounting for all trajectories was also defined by both Singh and O'Neill (2022) and Pan et al. (2017), although these studies focused on localized convection and the global atmospheric circulation, respectively.

In this paper, we apply MAFALDA to a series of simulations with a range of constant SSTs to determine how SST affects the mechanical efficiency of TCs. The paper is organized as follows: in section 2 we describe our model setup, definitions of terms, and analysis procedure. We present our results in section 3, including both analyses of the whole TC circulation and separate analyses of the overturning circulation passing through the TC eyewall and of the TC rainband circulations. Finally, in section 4 we discuss our results in the context of previous studies and present some conclusions.

2. Experimental Design and Method

a. Experimental Design

(i) Axisymmetric Simulations For this study we use the Bryan Cloud Model 1 (CM1) (Bryan and Fritsch 2002; Bryan and Rotunno 2009), version 20.2. CM1 is a non-hydrostatic model and integrates the moist, compressible governing equations. Experiments are run on an f-plane at 20°N in a 1500 km × 25 km axisymmetric domain with a horizontal grid spacing of 1km. The domain has a vertically stretched grid spacing (Wilhelmson and Chen 1982), ranging from 50m at a height of 0km to 500m above 5.5km. Rayleigh damping layers are imposed in the top 3km and outer 100km of the domain. CM1 is run in the mesoscale modeling setup with a Bryan and Rotunno (2009) planetary boundary layer parametrization. The microphysics parametrization is the Morrison double-moment moisture scheme with graupel as the large-ice category. The radiation

scheme is the RRTMG scheme. Following Bretherton et al. (2005), we remove the diurnal and seasonal cycles from RRMTG by fixing the solar constant at 650.83 W m^{-2} and the solar zenith angle at 50.5°. The model includes dissipative heating and conserves energy and mass. It accounts for the heat capacity of hydrometeors in the equation set for moist microphysics (Bryan and Fritsch 2002), and includes vertical transport of energy associated with hydrometeor sedimentation, all of which improve the energy conservation of the model.

We conduct a series of 200-day simulations of TCs in radiative-convective equilibrium (RCE) with the lower boundary of the model in each set to a different, constant SST, ranging from 295K to 307.5K in steps of 0.5K. The model is initialized with a modified Rankine vortex[1] with a maximum wind speed of 15 m s^{-1} at a radius of 75km, a radial decay parameter of -0.35 between radii of 75km and 200km, and the radius of zero winds at 500km. The initial environmental state sounding for each simulation was constructed using the horizontal- and time-mean vertical profiles of potential temperature and water vapor mixing ratio from the last 20 days of a corresponding 100-day RCE simulation, together with an imposed zero-wind profile for the initial state.

(ii) RCE simulations Each 100-day RCE simulation had an SST that matched that of the corresponding axisymmetric simulation. Settings for the RCE simulations generally matched those of the axisymmetric simulations, except that the RCE simulations were conducted in a 120km x 120km doubly-periodic domain with a model top at 26km, 1km higher than for the axisymmetric simulations. This was due to the CM1 requirement that input environmental soundings, such as those constructed from these RCE simulations, must extend higher than the chosen model top. Since the domain was doubly-periodic, no lateral Rayleigh damping layer was imposed. The upper-level Rayleigh damping layer was 1km thicker than for the axisymmetric simulations, to ensure that it began at the same level. All RCE simulations were initialized with the Dunion (2011) moist tropical sounding. No initial perturbation was added to the domain. The Bryan and Rotunno (2009) planetary boundary layer parametrization, which was used for the axisymmetric simulations, could not be used for these simulations since it was developed for axisymmetry. Instead, the planetary boundary layer parametrization in these simulations was the Yonsei University parametrization (Hong et al. 2006).

---

[1]A Rankine vortex has Vr^{-1}=constant inside the radius of maximum winds (RMW) and Vr=constant outside the RMW. In a modified Rankine vortex, the latter relationship is modified to Vr^X=constant (Holland 1980). In our simulations, X is set to 0.35 (i.e., the radial decay parameter in CM1 was -0.35).

(iii) 500 parcels simulation In addition to the main axisymmetric simulations presented here, we additionally run a simulation that is identical to the axisymmetric simulation with an SST of 299.5K and includes 500 Lagrangian air parcels. This simulation is run for 100 days in total and is used to validate our analysis methodology, see section 2b. In this work, the SST of 299.5K is used as a reference SST for quantifying changes in variables in % K^{-1}, as described in section 3a, and so was also selected as the SST for our parcel simulation.

b. MAFALDA Procedure

(i) Selection of "single-eyewall" and "realistic" time periods Because axisymmetric simulated TCs can exhibit unphysical behavior (O'Neill and Chavas 2020), from each individual 200-day simulation we selected for our main analyses all non-overlapping 2-day-long periods where the radius of maximum azimuthal winds (RMW) did not exceed a threshold that we subjectively set to 30km. These are henceforth referred to as the "realistic" periods. The evolution of the RMW in two of the constant-SST experiments is shown in Fig. 1, as well as both the realistic periods that we selected from these simulations and the 30km threshold. This threshold was set based on our observations of how the RMW evolved in the different simulations, which often included periods where the RMW suddenly grew. During such periods, the TC was either undergoing an unrealistic, axisymmetric version of an eyewall replacement cycle (ERC), or was spinning up. The 30km threshold was chosen to exclude these periods while still yielding a nonzero number of realistic time periods for all experiments. We excluded the ERC and spinup periods in order to study approximately steady-state TCs, and because the unrealistic ERCs may influence the energetics of the TCs.

The analysis subdomain sometimes contained strong secondary eyewalls during the realistic periods. From the set of 2-day realistic periods for each simulation, we selected for additional analyses (see Figs. S1-S3 and Tables S1-S3 in the online Supplemental Material) one of these as the "single-eyewall" period, where there were no strong secondary eyewalls in the inner subdomain in which we performed our analysis, denoted by the gray shading in Fig. 1. This subdomain will be discussed later. To identify the single-eyewall periods, for each realistic period, we calculated the radius at which the minimum value of the time-mean streamfunction at a height of 2km occurred within the analysis subdomain. The single-eyewall period was the period during which

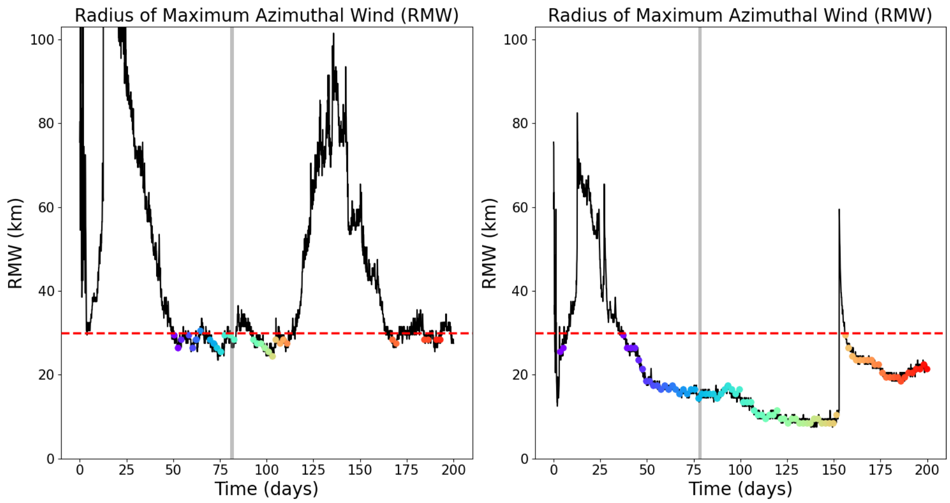

FIG. 1. Selected 2-day "realistic" (color-coded, pairs of rainbow points) and "single-eyewall" time periods (gray shading) for the simulations with an SST of 295K (left) and 305K (right). The RMW=30km threshold is denoted by the dotted red line. In both plots, the radius of maximum azimuthal wind at a height of 10m (RMW) is shown in black.

this minimum occurred at the smallest radius, on the condition that this radius was less than 100km (Fig. 2). The TC's time-mean eyewall at this height, which is associated with net upward vertical mass flux, should not extend further than the radius where the minimum in the time-mean Eulerian streamfunction occurs. As such, this radius presents an upper bound on the radial extent of the outer edge of the eyewall at this height. We implemented this restriction at a height above the boundary layer, so that this constraint would act at a height where the primary eyewall was present. Given this, we arbitrarily chose a height of 2km. This methodology provided an additional restriction that ensured that the strongest eyewall in the TC was the primary eyewall. As expected, the selected single-eyewall periods contained no strong secondary eyewalls in the analysis subdomain, whereas very strong secondary eyewalls existed in some realistic periods, which can be seen by inspection of the time-mean Eulerian streamfunctions (Fig. 2).

(ii) Reconstruction of thermodynamic cycles and mechanical efficiency derivation We analyzed the output data from our simulations during both the realistic and single-eyewall sets of 2-day time periods using the Mean Air Flow As Lagrangian Dynamics Approximation (MAFALDA). MAFALDA was initially developed by Pauluis (2016) for generalized convection, and was further developed for TCs by Mrowiec et al. (2016). MAFALDA involves four steps (Pauluis 2016):

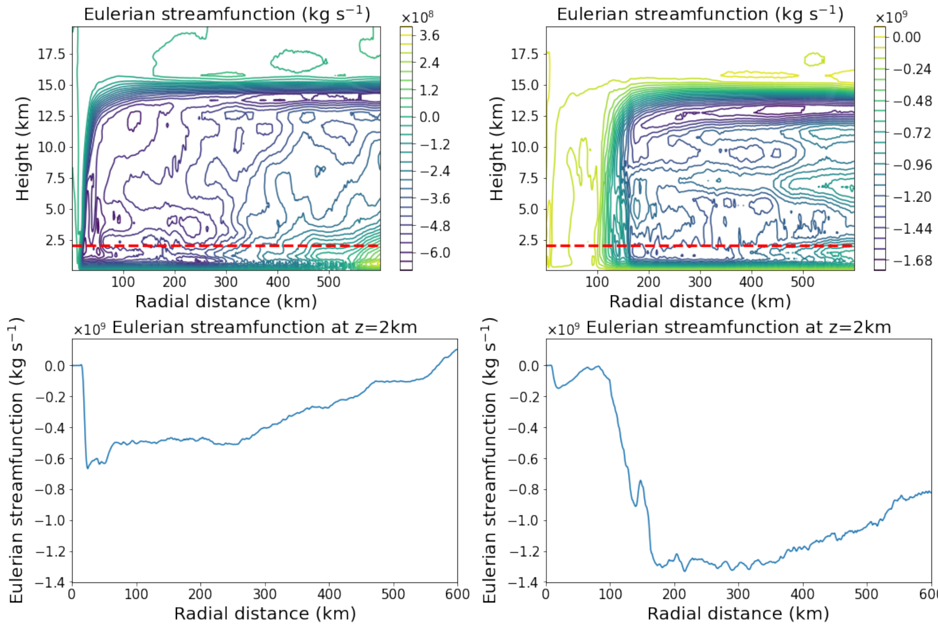

FIG. 2. Top: Time-mean Eulerian streamfunctions, calculated based on the density of dry air and the vertical and radial wind fields, for the single-eyewall period from the 305K simulation (left) and for a different, realistic time period from the same simulation. A height of 2km is indicated by the dashed red line on both plots. In this example, the TC contains a strong secondary eyewall during the realistic period that dominates over the primary eyewall, whereas it contains no strong secondary eyewalls during the single-eyewall period. Bottom: Corresponding values of the time-mean Eulerian streamfunctions at a height of 2km as a function of radius. Comparing the upper and lower plots demonstrates that, as expected, the radius where the minimum of the time-mean Eulerian streamfunction occurs acts as an upper bound on the radial extent of the strongest eyewall's outer edge at this height. For the single-eyewall periods, the minimum value in the time-mean Eulerian streamfunction at a height of 2km must occur at a radius of less than 100km. Given this condition, we pick the time period where this minimum occurs at the smallest radius.

1. Compute the TC's isentropic streamfunction, $\psi(z, \theta_e)$[2] (Fig. 3): the time-average of the net upward mass flux binned by the equivalent potential temperature value at each altitude (Pauluis and Mrowiec 2013; Mrowiec et al. 2016). For this, we compute the isentropic integral for an axisymmetric setup, where the differential area is equal to $r\,dr\,d\vartheta$. Here, r and ϑ represent the radial and azimuthal coordinates, respectively. We also integrate radially outward from the TC center to an outer radius R_{max} (the "subdomain"), which is equal to 600km for this study.

[2]We refer to ψ as the "isentropic" streamfunction following the standard terminology in the literature. However, it does not represent constant-entropy conditions.

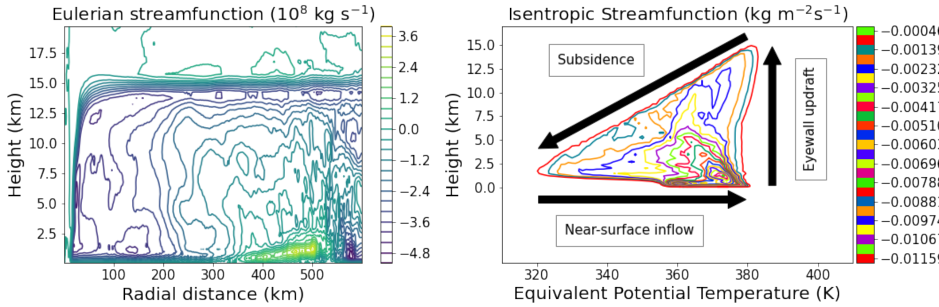

FIG. 3. Comparison of the time-mean Eulerian streamfunction (left), calculated based on the density of dry air and the vertical and radial wind fields; and the isentropic streamfunction, ψ (right) for the single-eyewall time period of the 305.5K simulation. Black arrows in the right-hand plot show the direction of the overturning circulation that passes through the eyewall in z-θ_e space. For the right-hand plot, each trajectory is color-coded according to the corresponding level of the isentropic streamfunction. Each of the levels of the isentropic streamfunction is associated with at least one "MAFALDA trajectory", which for many of the levels is quite large, as can be seen in the right-hand plot. However, the same plot shows that, due to the complexity of the TC circulation, some levels of ψ that contain one large MAFALDA trajectory sometimes also contain one or more, typically small, MAFALDA trajectories, as described in Section 2.

Since the TCs in the experiments with lower SSTs were smaller than at higher SSTs (see Fig. S4 in the online supplemental material), this constant radius was subjectively chosen so that it was not so large that it included too much of the environmental, or non-TC, circulation for the smallest storms and not so small that it missed important dynamics in the largest storms (see Text S1 in the online supplemental material).

2. Find the isentropic-mean values of thermodynamic variables, $\tilde{f}(z,\theta_e)$, defined as the mass weighted conditional average of the variable f.

3. Construct a set of N cyclic "trajectories" in z-θ_e coordinates from ψ, henceforth referred to as the "MAFALDA trajectories". These are the closed loops in z-θ_e space corresponding to the individual levels of ψ when plotted as a contour plot with N levels. There may be more than one MAFALDA trajectory for a given level of the streamfunction (Fig. 3). While MAFALDA trajectories account for the mean flow in z-θ_e coordinates, they do not necessarily capture the trajectory of any individual air parcel. However, we implicitly assume this in using MAFALDA (Pauluis and Mrowiec 2013; Pauluis 2016). Figure 4 presents a comparison

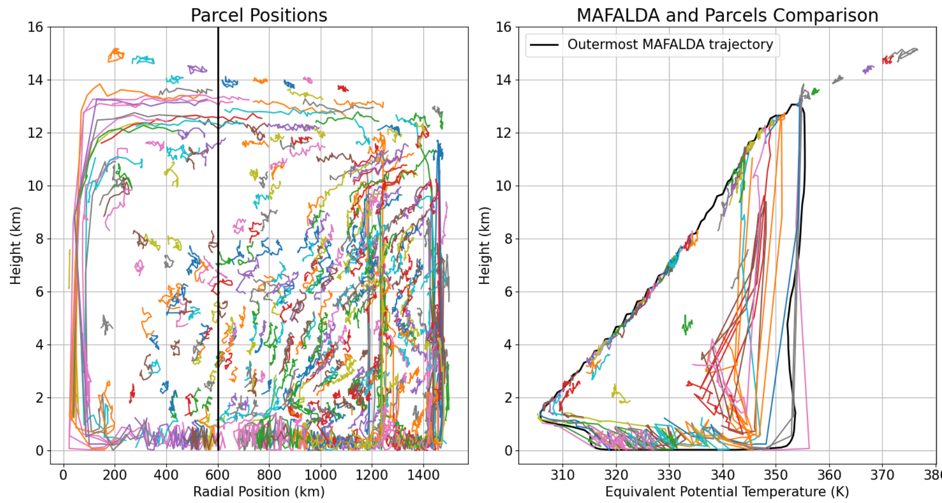

Fig. 4. Left: Trajectories of all 500 parcels during a 2-day period from an 100-day simulation with the same setup as the main simulation with an SST of 299.5K. Each parcel trajectory is color-coded. The black vertical line indicates the radial extent of the analysis subdomain. Right: Trajectories of parcels within the analysis subdomain only, during the chosen 2-day period, cast into height-equivalent potential temperature space. Each parcel trajectory is color-coded. The black line indicates the outermost MAFALDA trajectory derived from the isentropic streamfunction that was calculated during this period.

between the trajectories of Lagrangian air parcels in z-θ_e space and the largest MAFALDA trajectory derived from a 2-day period in the simulation with 500 parcels. This 2-day period met the requirements applied to select the realistic periods from the main simulations. For this comparison, we used only the trajectories of air parcels that were within the analysis subdomain ($r \leq R_{max}$) during this time. By visual inspection, the MAFALDA trajectories derived from the isentropic streamfunction provide a good approximation to the trajectories of real air parcels in the TC.

4. Interpolate the values of the thermodynamic variables, f, along the MAFALDA trajectories using the isentropic-mean variables, $\tilde{f}(z, \theta_e)$, as a starting point. This results in a "timeseries" of these variables following along each MAFALDA trajectory. These "timeseries" can be used to cast ψ into other thermodynamic spaces, for example temperature-entropy space.

MAFALDA allows us to quantify the mechanical efficiency of simulated TCs, as a function of energy reservoirs within the system. These include:

1. W_{Max}, equivalent to the useful work that a Carnot engine would produce if it were operating in equivalent temperature and entropy conditions (Pauluis 2016). It can also be thought of as the net heat energy gained by the TC including all heat sources and sinks (Fang et al. 2019), which can then be used either as kinetic energy of the TC's wind field or may be consumed by moist processes in the TC.

2. W_{KE}, the total kinetic energy generated along the MAFALDA trajectories. The net heat energy gained by the TC W_{Max} acts as a maximum bound on W_{KE}. The generated W_{KE} is dissipated by viscosity along the same trajectory that generates it. In a steady state, the generation of W_{KE} and its dissipation by viscosity are equal.

3. W_{Moist}, a two-part energetic penalty on W_{KE} due to the presence of moisture in a TC (Pauluis 2016; Pauluis and Zhang 2017) that acts to reduce W_{KE} compared to its maximum bound, the net heat energy gained by the TC W_{Max}. W_{Moist} is the sum of W_P and ΔG, and can be thought of as relating approximately to the irreversible entropy production from moist processes in the TC.

4. W_P, the energy that is used to lift water mass from where it enters the TC system —typically the surface—to the level where it leaves the system as precipitation. This term can be conceptualized as relating to irreversible entropy production from precipitation-associated dissipation in the TC (Pauluis et al. 2000; Pauluis and Held 2002a,b).

5. ΔG, the Gibbs penalty, representing the energetic cost of maintaining the TC hydrological cycle and associated phase transitions in subsaturated or supersaturated conditions (Pauluis 2011; Pauluis and Zhang 2017). The main contributor to ΔG is the entropy production by irreversible evaporation. Although the remainder of ΔG does not relate directly to moist irreversible entropy production, this term can still be thought of as approximately relating to irreversible entropy production due to the phase transitions of water in subsaturated or supersaturated conditions (Pauluis and Held 2002a,b).

All quantities are in J kg^{-1}, measured as per unit mass of dry air circulating in each "cycle", or level, of the isentropic streamfunction.

In order to construct a mechanical efficiency—and related energetic quantities—that reflect the energetics of the TC's whole circulation in the analysis subdomain, we must begin by calculating these variables for each MAFALDA trajectory separately. For a given MAFALDA trajectory, j, we obtain "timeseries" of thermodynamic quantities (e.g. the temperature $\tilde{T}$) following each trajectory. Given the set of timeseries derived for a specific trajectory, j, we can calculate the energetic quantities as in Pauluis (2016):

$$\begin{aligned} W_{Max,j} &= \oint \tilde{T} d\tilde{s} \\ \Delta G_j &= -\oint \sum_{w=v,l,i} \tilde{g_w} d\tilde{r_w} \\ W_{P,j} &= \oint \Gamma \tilde{r}_t d\tilde{z} \\ W_{KE,j} &= -\oint \tilde{\alpha_d} d\tilde{p} - W_{P,j} \end{aligned} \tag{1}$$

T is the absolute temperature, s is the moist entropy per unit mass of dry air, α_d is the specific volume per unit mass of dry air, p is the pressure, r_v, r_l, and r_i are the mixing ratios of water in its vapor, liquid, and solid phases, respectively, and g_v, g_l, and g_i are the specific Gibbs free energies of water in its vapor, liquid, and solid phases, respectively. Γ is the acceleration due to gravity and $r_t = r_v + r_l + r_i$ is the total mixing ratio of water. All thermodynamic variables are defined in Appendix A.

The first and second laws of thermodynamics can be combined to derive the Gibbs relationship (Pauluis 2011, 2016):

$$T ds = dh - \alpha_d dp - \sum_{w=v,l,i} g_w dr_w, \tag{2}$$

where h is the total enthalpy per unit mass of dry air, defined as in Pauluis and Zhang (2017).

Based on this relationship, the energetic quantities can be related to each other as follows:

$$W_{Max,j} = W_{KE,j} + W_{Moist,j}. \tag{3}$$

where

$$W_{Moist,j} = W_{P,j} + \Delta G_j \tag{4}$$

The kinetic energy generated along a trajectory, $W_{KE,j}$, is simultaneously dissipated by viscous forces. This dissipation can be represented by a quantity $D_{v,j} = \oint d\tilde{d}_v$, where d_v is the dissipation per unit mass of dry air (J/kg). Assuming the dissipation occurs mostly near the surface, the associated dissipation rate can be approximated by the bulk formula in Bister and Emanuel (1998)'s equation (6). Multiplying this by $\frac{1}{q_d}$, where q_d is the ratio of dry to total air mass, gives the dissipation rate per unit mass of dry air, which can then be used to calculate d_v. In steady state, $W_{KE,j} = D_{v,j}$.

Thus far, we have only defined the energetic quantities for a specific MAFALDA trajectory. We can now define energetic terms representing the whole circulation of the TC in the subdomain. We define the energetic quantities, X, for the TC circulation within our subdomain using the mean values of these quantities over all N levels of ψ:

$$X = \frac{\sum_{l=0}^{N} \sum_{j=0}^{M_l} X_{j,l}}{N} \tag{5}$$

Here, l represents each of the N levels of the isentropic streamfunction. As mentioned previously, due to the complexity of the TC circulation, several MAFALDA trajectories, j, may belong to the same level of the isentropic streamfunction (Fig. 3). Simply taking the mean over all MAFALDA trajectories would then weight levels of ψ containing more than one trajectory more heavily than others. Because, by construction, each level of ψ represents the same fraction of the mass transport (Pauluis 2016), we calculate the sum of each energetic quantity over all trajectories at a given level of ψ before taking the mean of each energetic variable over all levels.

Following (3) and (4), we can relate these mean energetic quantities to each other as (Pauluis 2016; Fang et al. 2019):

$$W_{Max} = W_{KE} + W_{Moist}. \tag{6}$$

where

$$W_{Moist} = W_P + \Delta G \tag{7}$$

MAFALDA additionally allows us to calculate the mean heat input and output to the TC circulation, Q_{in} and Q_{out}, defined as:

$$Q_{in} = \frac{\sum_{l=0}^{N}\sum_{j=0}^{M_l} Q_{in,j,l}}{N}$$
$$Q_{out} = \frac{\sum_{l=0}^{N}\sum_{j=0}^{M_l} Q_{out,j,l}}{N}$$

where:

$$d\tilde{q} = \tilde{T}d\tilde{s} + \sum_{w=v,l,i} \tilde{g_w} d\tilde{r_w}$$
$$Q_{in,j} = \oint d\tilde{q}\Big|_{d\tilde{q}>0}$$
$$Q_{out,j} = \oint d\tilde{q}\Big|_{d\tilde{q}<0}$$

Here, $d\tilde{q}$ represents the external heating of an air parcel. Q_{in} and Q_{out} account for all sources and sinks, respectively, of heat in the TC, including heating or cooling from phase transitions of water vapor and from surface heat flux. Finally, we define the mechanical efficiency, η_{mech}, of the TC following Pauluis and Zhang (2017):

$$\eta_{mech} = \frac{W_{KE}}{Q_{in}}, \quad (8)$$

Pauluis and Zhang (2017) demonstrated that the Carnot efficiency is an upper bound on η_{mech}. The Carnot efficiency is defined as:

$$\eta_C = \frac{T_{in} - T_{out}}{T_{in}}, \quad (9)$$

T_{in} and T_{out} are, respectively, the mean temperatures at which heat enters and leaves the TC system. They are defined based on Q_{in} and Q_{out}, following Pauluis and Zhang (2017):

$$T_{in} = \frac{Q_{in}}{\frac{Q_{in}}{T_{in}}},$$

where:

$$\frac{Q_{in}}{T_{in}}|_j = \oint \frac{d\tilde{q}}{\tilde{T}}\Big|_{\frac{d\tilde{q}}{\tilde{T}}>0},$$
$$\frac{Q_{in}}{T_{in}} = \frac{\sum_{l=0}^{N}\sum_{j=0}^{M_l}\frac{Q_{in}}{T_{in}}|_{j,l}}{N},$$

and T_{out} is defined similarly.

Henceforth, unless stated otherwise, all MAFALDA-derived energetic variables are calculated in J kg^{-1}. In some instances, we additionally calculate MAFALDA-derived energetic variables, X, in W m^{-2}, defined as (Pauluis 2016):

$$X(Wm^{-2}) = \sum_{l=0}^{N}\sum_{j=0}^{M_l}\Delta\psi_l X_{j,l}, \tag{10}$$

where $\Delta\psi_l$ is the mass circulation (kg m^{-2} s^{-1}) at each level of ψ, defined as follows (Pauluis 2016):

$$\Delta\psi_l = -N^{-1}\psi_{min}, \tag{11}$$

where ψ_{min} is the minimum value of ψ. $\Delta\psi_l$ has the same value for all levels by construction.

When using MAFALDA, isolating the thermodynamic cycles associated with the TC from cycles associated with convection far from the center requires a choice of outer radius, which defines the subdomain in which we reconstruct these cycles. For this study, the outer radius was 600km (see Text S1, Table S4, and Fig. S4 in the online supplemental material). We checked the sensitivity of the results derived from the realistic and single-eyewall periods to the outer radius, considering values between 400km and 1200km (see Text S1 and Tables S5-S14 in the online supplemental material). In general, the signs and statistical significance of trends in the variables with increasing SST are not sensitive to the choice of outer radius. In the following two sections, we will note instances where the sign or statistical significance of a trend is not robust to the choice of outer radius.

3. Results

a. Variability of the MAFALDA-derived variables for the whole TC circulation

We first examine how the mechanical efficiency of the whole TC circulation within the subdomain varies with SST, as well as the variability of related energetic quantities. These results are presented as black boxplots and trend lines in figures 5 and 6. For each boxplot, the unfilled circles represent outlier points, which are separated from the median value by more than 1.5 interquartile ranges. Only the results from the realistic periods will be discussed in the remainder of this text—results from the single-eyewall periods are presented in the online supplemental material. Henceforth, all trends are quantified in units of % K^{-1}, calculated for the realistic periods as percentages of the mean value of each variable at a reference SST of 299.5K. This SST is closest to the most recently-published global SST threshold for TC genesis (26.4°C) (Defforge and Merlis 2017).

W_{KE} increases with SST at 3.4 % K^{-1} (Fig. 5, Table 1). Accompanying this, the net heat energy gained by the TC, W_{Max}, increases at a higher rate of 7.0 % K^{-1}. We also observe a strong increase in moist processes with SST, associated with the increase in atmospheric moisture implied by Clausius-Clapeyron scaling at constant relative humidity of about 7 % K^{-1} (Trenberth et al. 2003). The related increased irreversibility is reflected by an increase in the associated energetic penalty, W_{Moist}, of 9.6 % K^{-1}. Because of this strong increase, W_{Moist} represents a larger portion of W_{Max} at higher SST. This reduces the magnitude of the 3.4 % K^{-1} increase in W_{KE} compared to the 7.0 % K^{-1} increase in its maximum bound, the net heat energy gained by the TC, W_{Max}.

The 9.6 % K^{-1} W_{Moist} increase exceeds the Clausius-Clapeyron scaling of 7 % K^{-1} that applies to the atmospheric water content. This is because this energetic penalty is not only dependent on changes in atmospheric moisture content: it is also dependent on changes in the depth of the circulation, and changes in the Gibbs free energy of water in all its phases—as can be seen by the definitions of W_P and ΔG. Changes in relative humidity may also play a role in the magnitude of the increase.

Additionally, both components of W_{Moist}, W_P and ΔG, increase with SST, at 12 % K^{-1} and 8.2 % K^{-1}, respectively (Fig. 6, Table 1). Since W_P is related to the precipitation in the TC, the increase in W_P may reflect an increase in TC precipitation with SST.

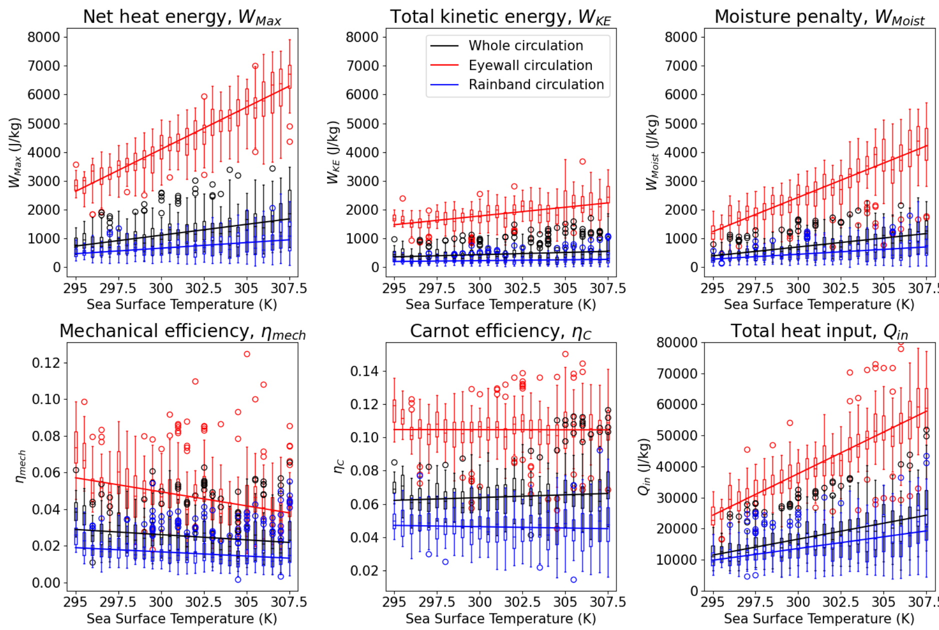

FIG. 5. Top: W_{Max}, W_{KE}, and W_{Moist} versus SST. Bottom: η_{mech}, η_C, and Q_{in} versus SST. Results are derived from the set of realistic periods. Several realistic periods were chosen for each simulation, as described in Section 2b. The boxplots in this figure show the spread of the results calculated for all realistic periods from each simulation. Black boxplots and trend lines are for the whole circulation of the TCs, red boxplots and trend lines are for the eyewall circulation only, and blue boxplots and trend lines are for the rainband circulation only. For each boxplot, the unfilled circles represent outlier points. Outlier points are identified as those that are separated from the median value by more than 1.5 interquartile ranges.

In spite of the increase in W_{KE} with SST, the mechanical efficiency decreases at -2.1 % K^{-1} (Fig. 5, Table 1). This is due to the increase in the heat input Q_{in}, which grows at 6.3 % K^{-1}. Although the increase in W_{KE} acts to increase the mechanical efficiency, the increase in Q_{in} acts to decrease it, as can be seen from equation (8). Here, the effect of the increase in the heat input dominates, resulting in a decreased mechanical efficiency.

In contrast, the Carnot efficiency, η_C, increases with SST at a rate of 0.53 % K^{-1}[3] (Fig. 5, Table 1). The increase in η_C is due to the increase in T_{in}-T_{out} of 0.86 % K^{-1}[4], which dominates over the 0.32 % K^{-1} increase in the input temperature, T_{in} (Table 2, Fig. 7). Because η_{mech} decreases while

[3]The Carnot efficiency trend changes sign at large outer radius values, and its statistical significance is somewhat sensitive to outer radius (Table S5)

[4]The T_{in}-T_{out} trend changes sign at large outer radius values, and its statistical significance is somewhat sensitive to outer radius (Table S5)

TABLE 1. Trends for the MAFALDA-derived energetic and efficiency variables during all realistic periods. Values are shown for the whole circulation of the TCs, as well as for only the eyewall and rainband circulations. All linear trend values are statistically significantly different from zero at the 99 % confidence level except for the eyewall η_C trend, which is not statistically significant, and the rainband η_C, which is statistically significantly different from zero at only the 90 % confidence level. To determine this, we used a two-sided t-test, using the HC1 estimator (MacKinnon and White 1985) to correct for heteroskedasticity (Text S3 in the online supplemental material).

Variable	Circulation type	Trend (% K^{-1})
W_{Max}	Whole	7.0
	Eyewall	7.8
	Rainband	6.8
W_{KE}	Whole	3.4
	Eyewall	3.5
	Rainband	2.8
W_{Moist}	Whole	9.6
	Eyewall	11
	Rainband	9.3
W_P	Whole	12
	Eyewall	14
	Rainband	12
ΔG	Whole	8.2
	Eyewall	9.7
	Rainband	7.5
Q_{in}	Whole	6.3
	Eyewall	7.4
	Rainband	5.9
η_{mech}	Whole	-2.1
	Eyewall	-3.2
	Rainband	-2.8
η_C	Whole	0.53
	Eyewall	-0.013
	Rainband	-0.37
$\frac{\eta_{mech}}{\eta_C}$	Whole	-2.7
	Eyewall	-3.0
	Rainband	-2.2

η_C increases with SST, the ratio $\frac{\eta_{mech}}{\eta_C}$—the "relative efficiency"—decreases at -2.7 % K^{-1} (Fig. 7, Table 1).

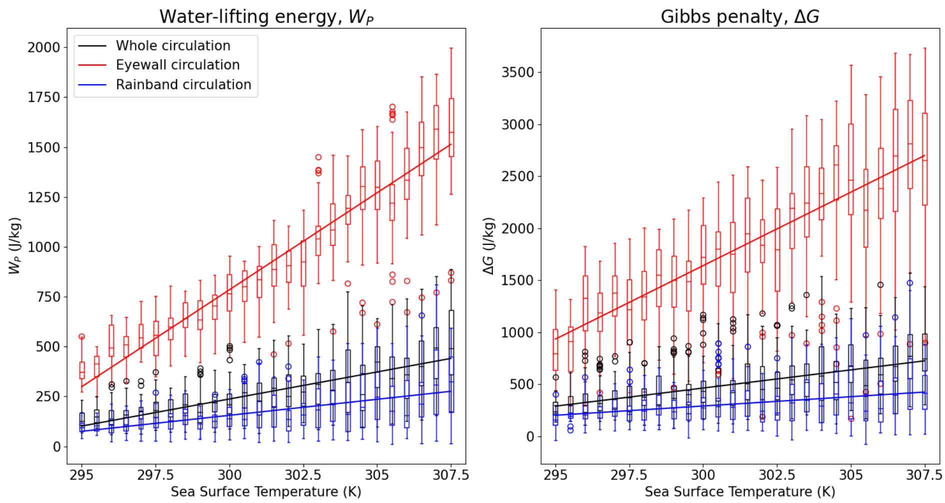

FIG. 6. W_P and ΔG versus SST. Results are derived from the set of realistic periods. Black boxplots and trend lines are for the whole circulation of the TCs, red boxplots and trend lines are for the eyewall circulation only, and blue boxplots and trend lines are for the rainband circulation only. For each boxplot, the unfilled circles represent outlier points. Outlier points are identified as those that are separated from the median value by more than 1.5 interquartile ranges.

b. Effect of SST on the eyewall and rainband circulations

In addition to our analysis of the mean behavior of energetic and efficiency quantities for the TC's whole circulation, we differentiate between the more efficient eyewall circulation and the circulation in the non-eyewall rainbands[5] (Text S2). Because the TC eyewall is uniquely saturated and characterized by the deepest convection within the storm, this aspect of the TC circulation may respond quite differently to changes in SST compared to the rainband circulation. The eyewall circulation results are shown as red boxplots and trend lines in Figures 5-7, whereas the rainband circulation results are color-coded in blue. Changes in energetic and efficiency variables for the eyewall and rainband circulations are consistently of the same sign as changes for the whole circulation (Figs. 5-7, Table 1) and are highly significant, with the exception of η_C for both the eyewall and rainband circulations.

[5]While the equality in equation (3) holds well—to within 5%—for most of the time periods we examine, it occasionally holds to within only 10%. For the single-eyewall periods, this is the case for several MAFALDA trajectories belonging to levels of ψ corresponding to the rainband circulation for the 295K simulation, and for trajectories at one level belonging to the rainband circulation for the 296K simulation. For the realistic periods, (3) holds to within only 10% for the eyewall circulation in 5 of the 1835 total realistic periods examined across all simulations, and in one realistic period for both the whole and rainband circulations. Additionally, in one of the realistic periods, the equality does not hold for the eyewall circulation.

The -3.2 % K^{-1} decrease in the mechanical efficiency of the eyewall circulation is of a similar size as the -2.8 % K^{-1} decrease in the mechanical efficiency of the rainband circulation (Fig. 5, Table 1), although the absolute magnitude of the decrease for the eyewall circulation is larger, as can be seen by inspection of Fig. 5. Accompanying these decreases, the Carnot efficiency for the eyewall circulation does not statistically significantly change[6], whereas the Carnot efficiency of the rainband circulation decreases with a weak level of statistical signficance at -0.37 % K^{-1}[7]. Because of this, the decrease in the relative efficiency is more pronounced for the eyewall circulation, at -3.0 % K^{-1}, than the -2.2 % K^{-1} decrease for the rainband circulation (Table 1). As a result, there is a smaller difference between the relative efficiencies of the eyewall and rainband circulations at higher SST (Fig. 7).

c. Variability of quantities related to the MAFALDA-derived energetic terms

Finally, we examine the variability of more familiar terms in our experiments that relate to the MAFALDA-derived energetic quantities (Fig. 7, Table 2). We examine the variability of the kinetic energy (KE) per unit mass of dry air based on the maximum azimuthal wind speed at 10m, v_{max}, in each experiment, defined in Appendix B. Dry air was used as the reference air mass to provide a meaningful comparison to the MAFALDA-derived energetic quantities, which are also defined per unit dry air mass. We used a similar definition for the KE per unit mass of dry air based instead on the potential intensity, v_{PI}, which is an upper bound on v_{max} (Emanuel 1986; Bister and Emanuel 1998) (Appendix B). We additionally examine the variability with SST of the integrated kinetic energy (IKE) (Powell and Reinhold 2007), surface precipitation rate, and surface total, latent, and sensible heat fluxes (Appendix B). All quantities are computed only within the subdomain that we used to calculate the MAFALDA-derived energetic and efficiency variables.

The KE associated with v_{max} increases at a rate of 5.1 % K^{-1} with SST (Fig. 7, Table 2). Accompanying the increase in the v_{max}-associated KE, the KE associated with the potential intensity, v_{PI}, also increases at a rate of 6.8 % K^{-1}. The 6.8 % K^{-1} increase in the v_{PI}-associated KE is very close to the increase in W_{Max} of 7.0 % K^{-1} that we observe for the whole circulation (Table 1). Additionally, the increase in the v_{max}-associated KE of 5.1 % K^{-1} is reduced compared to the 6.8 % K^{-1} increase in the v_{PI}-associated KE, similar to the reduced magnitude of the

[6]The sign and statistical significance of the eyewall trend are sensitive to outer radius (Table S6)
[7]The statistical significance and sign of the rainband trend are somewhat sensitive to outer radius (Table S7)

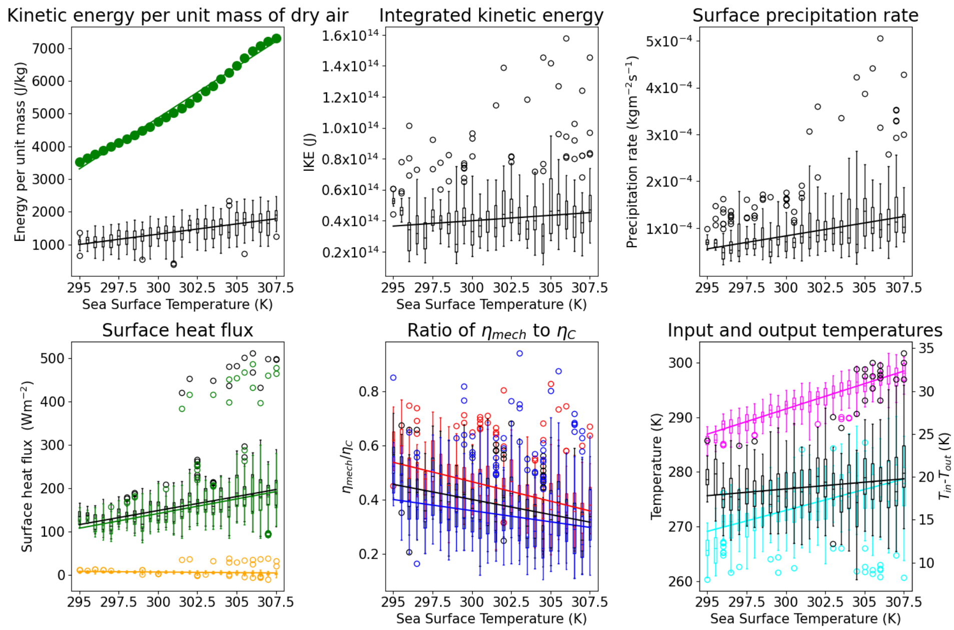

FIG. 7. Top: Maximum tangential wind speed-derived (black) and potential intensity-derived (green) kinetic energy per unit mass of dry air, integrated kinetic energy (IKE), and surface precipitation rate versus SST. Bottom left: Surface sensible (orange), latent (green), and total (black) heat flux versus SST. Bottom center: η_{mech}/η_C for the whole circulation (black), eyewall circulation (red), and rainband circulation (blue) versus SST. Bottom right: temperatures associated with the heat input (magenta) and output (cyan), as well as the difference between these temperatures (black), for the whole circulation of the TC heat engine, versus SST. Results for all variables except the potential intensity-derived kinetic energy are calculated for the realistic periods. The potential intensity-derived kinetic energy is calculated with output from our RCE simulations and so is not specific to any given time period from each simulation. For each boxplot, the unfilled circles represent outlier points. Outlier points are identified as those that are separated from the median value by more than 1.5 interquartile ranges.

increase in W_{KE} compared to the increase in W_{Max} that we observe for all circulation types (Table 1). Finally, the IKE, which accounts for the full 10-meter wind field of the TC in the subdomain, also increases at 1.6 % K^{-1}. These results are all in qualitative agreement with the increases in W_{KE} that we observed for all circulation types (Fig. 5, Table 1).

The surface precipitation rate increases with SST at 6.5 % K^{-1} (Fig. 7, Table 2). This is consistent with the 12 % K^{-1} increase in W_P (Fig. 6, Table 1).

The total surface heat flux (THF), which represents a portion of the total heating of the TC, Q_{in}, increases at 4.3 % K^{-1} with SST (Fig. 7, Table 2). In order to make a meaningful comparison

TABLE 2. Trends for quantities related to the MAFALDA-derived variables during the realistic periods, as well as for MAFALDA-derived temperature variables calculated for the whole circulation during the realistic periods. The potential intensity-derived kinetic energy is calculated from the output of RCE simulations and so is not calculated during the realistic periods. All trend values are constructed from a linear fit to the data and are calculated as percentages of the mean value of each variable at an SST of 299.5K. All linear trend values are statistically significantly different from zero at the 99 % confidence level. To determine this, we used a two-sided t-test, using the HC1 estimator (MacKinnon and White 1985) to correct for heteroskedasticity (Text S3 in the online supplemental material).

Variable	Trend (% K^{-1})
Kinetic energy derived from v_{max}	5.1
Kinetic energy derived from v_{PI}	6.8
Integrated Kinetic Energy	1.6
Surface precipitation rate	6.5
Total surface heat flux	4.3
Surface latent heat flux	4.7
Surface sensible heat flux	-4.0
Input temperature, T_{in}	0.32
Output temperature, T_{out}	0.28
T_{in}-T_{out}	0.86

between the changes in the surface heat fluxes and the response of Q_{in} to SST, we additionally calculated the trend in Q_{in} when this variable was instead computed in W m^{-2} rather than in J kg^{-1}. Q_{in} (W m^{-2}) increases at 6.4 % K^{-1} (Table 3), in agreement with the increase in the THF. While the THF increases with SST, its latent and sensible components show opposite-signed changes with SST. The surface latent heat flux (LHF) increases at 4.7 % K^{-1}, but the surface sensible heat flux (SHF) decreases at -4.0 % K^{-1}. This difference may be due to the moistening of the atmosphere implied by Clausius-Clapeyron scaling as SST increases. Singh and O'Neill (2022) found, in radiative-convective equilibrium (RCE) experiments of localized convection, that the SHF was larger in dry RCE than in moist RCE. Because the SHF represents a small portion of the THF (Fig. 7), the change in the THF is almost entirely due to the increase in the LHF. This increase in the LHF with SST is qualitatively consistent with Clausius-Clapeyron scaling, at constant near-surface relative humidity, of the mixing ratios in the LHF bulk formula shown in Appendix B.

Table 3. Trends for the MAFALDA-derived energetic variables, calculated in W m^{-2} during all realistic periods. Values are shown for the whole circulation of the TCs only. All linear trend values are statistically significantly different from zero at the 99 % confidence level. To determine this, we used a two-sided t-test, using the HC1 estimator (MacKinnon and White 1985) to correct for heteroskedasticity (Text S3 in the online supplemental material).

Variable	Circulation type	Trend (% K^{-1})
W_{KE}	Whole	3.9
W_P	Whole	12
ΔG	Whole	8.3
Q_{in}	Whole	6.4

4. Discussion

We have investigated how the mechanical efficiency, η_{mech}, of mature tropical cyclones is affected by sea surface temperature (SST). We found that η_{mech} decreases with SST, at a rate of -2.1 % K^{-1} (Table 1). This decrease was driven by a 6.3 % K^{-1} increase in the total heating of the TC, Q_{in}, that dominates over the 3.4 % K^{-1} increase in the kinetic energy of the wind field, W_{KE}. The increase in W_{KE} is smaller than the 7.0 % K^{-1} increase in its maximum bound, the net heat energy gained by the TC W_{Max}. The majority of the increase in the net heat energy is instead reflected by the strong increase in the moist processes in the TC. This increase occurs in part because of an increase in the atmospheric moisture content that is expected from Clausius-Clapeyron scaling. The related larger irreversibility at higher SST is shown by the increase in the associated moisture penalty, W_{Moist}, of 9.6 % K^{-1}. W_{Moist} represents a larger portion of W_{Max} at higher SST, which reduces the magnitude of the increase in W_{KE} compared to the increase in W_{Max}. This is true regardless of the subset of the TC circulation that we consider (Table 1, Figure 5).

In contrast to our results, Pan et al. (2017) find, using primarily the NCEP-DOE R2 (Kalnay et al. 1996; Kistler et al. 2001; Kanamitsu et al. 2002) and ERA-Interim (Uppala et al. 2005; Berrisford et al. 2011; Dee et al. 2011) reanalysis datasets, that the mechanical efficiency of the global atmosphere increased over the period 1979-2013. However, reanalysis products are not well suited to evaluating climate trends (Thorne and Vose 2010; Chemke and Polvani 2019). Together with the fact that the global atmospheric heat engine and the TC heat engine may behave quite differently in response to warming, this may help explain the discrepancy between our results and theirs.

An upper bound of the mechanical efficiency is the Carnot efficiency, η_C. In our simulations, η_C increases with SST at a rate of 0.53 % K^{-1} (Table 1), inconsistent with previous studies of the global atmosphere (Lembo et al. 2019; Lucarini et al. 2010a,b; Knietzsch et al. 2015). However, the responses to warming of the TC heat engine and global atmospheric heat engine may be quite different. The increase in the Carnot efficiency combined with the decrease in the mechanical efficiency results in a decrease of -2.7 % K^{-1} in the relative efficiency, $\frac{\eta_{mech}}{\eta_C}$. Because this decrease is more pronounced for the eyewall circulation, at -3.0 % K^{-1}, than the -2.2 % K^{-1} decrease for the rainband circulation, there is a smaller difference between the relative efficiencies of the eyewall and rainband circulations at higher SST (Fig. 7). The relative efficiency of the whole circulation ranges from about 0.2 to 0.6 for the majority of the periods examined. Ozawa and Shimokawa (2015) used observations of 663 North Pacific TCs to estimate the relative efficiency of a TC to be about 0.6 on average. Although our relative efficiency values generally fall below 0.6, our TC relative efficiency is consistently greater than the estimated relative efficiency of the global atmosphere of 0.1 (Golitsyn 1970), which is in agreement with Ozawa and Shimokawa (2015). Our results may differ with those of Ozawa and Shimokawa (2015) for several reasons: first, the authors assumed a uniform surface wind speed in their estimation of the relative efficiency, which is not the case in reality; second, we examine highly idealized, axisymmetric TCs whereas Ozawa and Shimokawa (2015) used data from real TCs. It is possible that the asymmetric aspects of the TC circulation, or other factors such as interactions between TCs and their environment, are important in setting the relative efficiency of real TCs.

W_{KE} increases with SST at a rate of 3.4 % K^{-1} (Table 1, Fig. 5). This increase is consistent across all circulation types[8]. An increase in the kinetic energy is also supported by a 5.1 % K^{-1} increase in the v_{max}-associated KE, and by a 1.6 % K^{-1} increase in the IKE (Table 2). These increases are consistent with the increases in comparable or related quantities with SST found in many previous studies of the global atmosphere (Lembo et al. 2019; Pan et al. 2017), of localized convection (Romps 2008; Singh and O'Gorman 2016; Pauluis 2016), and of TCs (Wang and Toumi 2021; Kreussler et al. 2021; Khairoutdinov and Emanuel 2013; Knutson and Tuleya 2004), although some studies of the global atmosphere instead find a decrease in similar variables (LaLiberté et al. 2015;

[8]The rainband trend changes sign at large outer radius values, and its statistical significance is sensitive to outer radius (Table S7)

Lucarini et al. 2010a,b; Knietzsch et al. 2015). In particular, the increase in W_{KE} is comparable to a key result of Khairoutdinov and Emanuel (2013), who study how the kinetic energy per unit area per storm varies across a series of constant-SST "TC-world" experiments. Across a suite of these simulations, the SST varied from 294-309K. They found that the kinetic energy (KE) per unit area at the surface per storm increased dramatically with SST, at a rate of about 17 % K^{-1}.

The magnitude of the increase in W_{KE} is consistently lower than the increase in W_{Max} for all circulation types (Table 1). This is due to a strong increase in the energetic penalty associated with moist irreversible entropy production in a TC, W_{Moist}. The increase in W_{Moist} is in agreement with the increases of comparable quantities in previous studies of the global atmosphere and of localized convection (Singh and O'Gorman 2016; Lembo et al. 2019; Romps 2008; Knietzsch et al. 2015; Pauluis 2016).

Both components of the moisture penalty—the precipitation-associated portion, W_P, and the portion associated with the TC hydrological cycle, ΔG—increase with SST, at 12 % K^{-1} and 8.2 % K^{-1}, respectively (Fig. 6, Table 1). This is true for all circulation types, and is qualitatively in agreement with increases in similar quantities found in studies of both localized convection and the global atmosphere (LaLiberté et al. 2015; Singh and O'Gorman 2016; Romps 2008; Pauluis 2016). The increase in W_P is associated with an increase in the surface precipitation rate of 6.5 % K^{-1} (Table 2), consistent with the results of previous studies for both TCs and the global atmosphere (Knutson and Tuleya 2004; Jeevanjee and Romps 2018; Khairoutdinov and Emanuel 2013). W_P increases more strongly than the surface precipitation rate with SST, which may be due to some portion of the precipitation re-evaporating before it reaches the surface, so that some of the increase in the total precipitation would be reflected in W_P but not in the surface precipitation rate. W_P also depends on the depth of the TC circulation, which increases with SST (See Fig. S4 in the online supplemental material).

Finally, the -2.1 % K^{-1} decrease in the mechanical efficiency occurs in spite of the increase in W_{KE} due to an accompanying 6.3 % K^{-1} increase in the heat input, Q_{in} (Table 1). Recall that Q_{in} does not only include the surface heat fluxes- it also accounts for radiative heating, heating due to the phase transitions of water vapor, and dissipative heating associated with both precipitation and kinetic energy dissipation. In what follows, we will examine further the increase in the heat input with SST, where all variables are calculated in W m^{-2} for consistency. Motivated by the strong role of moisture in modulating the kinetic energy increase, we examine separately the variability with SST of different "moist" and "dry" heat sources that contribute to the 6.4 % K^{-1} increase in Q_{in} (W m^{-2}) (Tables 2 and 3). The total surface heat flux should represent the majority of Q_{in}. We find that the increase in total surface heat flux of 4.3 % K^{-1} is almost entirely due to a 4.7 % K^{-1} increase in the surface latent heat flux, whereas the surface sensible heat flux exhibits a decrease of -4.0 % K^{-1} with SST. There is a noticeable difference in magnitude between the increase in the total surface heat flux and the increase in the total heating. We speculate that, based on the increases in W_{KE} (W m^{-2}) and W_P (W m^{-2}) of 3.9 % K^{-1} and 12 % K^{-1}, respectively, both the dissipative heating associated with dry frictional dissipation and the precipitation-associated dissipative heating increase with SST. However, these increases in dissipative heating alone are unlikely to explain the discrepancy between the increases in Q_{in} (W m^{-2}) and the total surface heat flux. Since Q_{in} also includes radiative heating, we postulate that an increase in radiative heating must occur with increasing SST, though calculating this with MAFALDA will be left for future work. In summary, the increase in Q_{in} with SST is dominated by the increases in the moist heat sources—surface latent heat flux and precipitation-associated dissipation—with additional positive contributions due to the dry heating sources from kinetic energy dissipation and a likely increase in radiative heating, whereas the decrease in the dry surface sensible heat flux acts to decrease Q_{in}.

Our experimental setup and analyses include several idealizations. A highly idealized aspect of our simulations is the assumption that TCs are axisymmetric, which is far from true in reality. Our results may omit important changes in the asymmetric circulation of TCs with SST. Our simulations also represent the ocean as a constant-SST surface, and so important feedbacks between the TC and the ocean are not captured in our simulations. Future studies should verify that our results are robust in less idealized models, including non-axisymmetric models. Importantly, our methodology assumes that the circulation of the TC in the subdomain where we perform our analysis is not open. However, this is far from the case in the real world, and even in our simulations. Future work should test whether our results are robust when analytical techniques that do not assume a closed circulation are used. Finally, the effect of SST on the global distribution and frequency of TCs was not considered in this study, since we only examined the impacts of SST on single TCs.

The conceptualization of the tropical cyclone as a heat engine has long been used to study factors affecting the intensity of TCs (e.g. Emanuel 1986; Bister and Emanuel 1998). The efficiency of the

TC heat engine is a key factor in determining how the intensity of TCs, as well as their full wind fields, vary in different climates. However, the frameworks used by many previous studies fail to fully account for the effects of moisture on the efficiency of TCs, and often focus on the changes in TC intensity or in the surface wind field, ignoring changes in other portions of the wind field (e.g. Emanuel 1986; Bister and Emanuel 1998; Wang and Toumi 2021; Kreussler et al. 2021). Despite the idealizations inherent to our model and analysis procedure, we conclude that the mechanical efficiency of mature TCs decreases with increasing SST. The large increase in moist processes and related irreversibility in the TC with SST results in the associated moisture penalty consuming a larger portion of the net heat energy gained by the TC, which also increases with SST, in warmer simulations. In this way, the increase in the moisture penalty modulates the magnitude of the increase in the kinetic energy produced by the TC heat engine. We also find that moist heating sources are the primary contributors to the large increase in the total heat input to the TC, which ultimately drives the decrease in the mechanical efficiency in spite of the increase in the kinetic energy. Our results highlight the importance of considering in full the effects of moisture on the TC heat engine in studies of the TC's relationship to climate.

Acknowledgments. We would like to thank Ipshita Dey and Hao Fu for their helpful comments on this work, as well as the staff of the Stanford Research Computing Center, who provided much assistance during this work, and who made it possible to carry out all of our simulations and computations via the use of their high-performance computing cluster. We are grateful to Bjorn Stevenson, whose open-source code we used to calculate saturation vapor pressure in our work. Finally, we would like to thank Tayden Li and Job Weaver of Stanford's Department of Statistics for their advice on the statistical treatment of our results.

Data availability statement. Modified source code and model inputs required to rerun our simulations can be found at `https://doi.org/10.5281/zenodo.7983011`. The CM1 homepage is `https://www2.mmm.ucar.edu/people/bryan/cm1/`, from where all other required inputs and source code can be downloaded. All analysis code is available at `https://doi.org/10.5281/zenodo.7302058`.

APPENDIX A

Definitions of thermodynamic quantities

Following Bolton (1980), the equivalent potential temperature, θ_e, is defined as follows:

$$\theta_e = T\left(\frac{p_{ref}}{p}\right)^{(0.2854(1.0-0.28r_v))} e^{\left(\frac{3376.0}{T_{LCL}}-2.54\right)r_v(1.0+0.81r_v)},$$

where T is the temperature (K), p_{ref} is a reference pressure, set to 1000hPa, p is the total pressure (hPa), r_v is the water vapor mixing ratio (kg kg^{-1}), and T_{LCL} is the temperature (K) at the lifting condensation level:

$$T_{LCL} = 55.0 + \frac{2840.0}{3.5\ln T - \ln(1.0\times10^{-20} + e_p) - 4.805}.$$

The water vapor pressure in hPa, e_p, is defined as:

$$e_p = \frac{p r_v}{\frac{R_d}{R_v} + r_v}.$$

R_d (J kg^{-1}K^{-1}) is the specific gas constant for dry air and R_v (J kg^{-1}K^{-1}) is the specific gas constant for water vapor.

Henceforth, unless noted otherwise, thermodynamic terms are defined following Pauluis (2016). Moist entropy, s (J kg^{-1}K^{-1}), per unit mass of dry air, is defined as:

$$
\begin{aligned}
s = s_d + r_v s_v + r_l s_l + r_i s_i \\
s_d = c_{p,d} \ln \frac{T}{T_{ref}} - R_d \ln \frac{p_d}{p_{ref}} \\
s_v = c_{p,l} \ln \frac{T}{T_{ref}} + \frac{L_v}{T} - R_v \ln \mathcal{H} \\
s_l = c_{p,l} \ln \frac{T}{T_{ref}} \\
s_i = c_{p,i} \ln \frac{T}{T_{ref}} - \frac{L_{f,0}}{T_{ref}}
\end{aligned}
$$

$c_{p,d}$, $c_{p,l}$, and $c_{p,i}$ (J kg^{-1}K^{-1}) are the specific heat capacities of dry air, liquid water, and ice, respectively. $L_{f,0}$ (J kg^{-1}) is the latent heat of freezing at 273.15K. T_{ref} (K) is the reference value of temperature, set here to 273.15K. $p_d = p - e_p$ is the partial pressure of dry air, while r_l and r_i (kg kg^{-1}) are the mixing ratios of water in its liquid and solid phase, respectively. L_v is the latent heat of vaporization as a function of temperature, defined as:

$$
L_v = L_{v,0} + (c_{p,v} - c_{p,l})(T - T_{ref})
$$

$L_{v,0}$ (J kg^{-1}) is the latent heat of vaporization at 273.15K and $c_{p,v}$ is the specific heat capacity of water vapor.

$\mathcal{H}$ is the relative humidity with respect to liquid water, defined as:

$$
\mathcal{H} = \frac{e_p}{e_s},
$$

where:

$$
e_s = min(e_{s,i}, e_{s,l}),
$$

where $e_{s,l}$ is the saturation vapor pressure with respect to liquid water and $e_{s,i}$ is the saturation vapor pressure with respect to solid water, where both are defined as in Goff and Gratch (1946).

Following convention, the entropy as defined here assumes that the specific entropies of dry air and of liquid water are zero in the reference state. A brief discussion of how the MAFALDA-derived variables depend on the choice of reference entropy can be found in Appendix C.

The specific volume per unit mass of dry air, α_d (m^3 kg^{-1}), is defined:

$$\alpha_d = \frac{R_d T + R_v r_v T}{p}.$$

The specific Gibbs free energy of water vapor, liquid water, and solid water (J kg^{-1}) are defined, respectively, as:

$$g_v = c_{p,l}(T - T_{ref} - T \ln \frac{T}{T_{ref}}) + R_v T \ln \mathcal{H}$$
$$g_l = c_{p,l}(T - T_{ref} - T \ln \frac{T}{T_{ref}})$$
$$g_i = c_{p,i}(T - T_{ref} - T \ln \frac{T}{T_{ref}}) - L_{f,0}(1 - \frac{T}{T_{ref}})$$

APPENDIX B

Definitions of quantities related to MAFALDA-derived variables

We define the kinetic energy per unit mass of dry air based on the maximum tangential wind speed at a height of 10m, v_{max} (m s^{-1}). The reference mass was that of dry air to ease comparison with the MAFALDA- derived energetic quantities, which are defined per unit mass of dry air. The v_{max}-derived kinetic energy is defined as:

$$KE_{v_{max}} = \frac{1}{2} \frac{\rho_m}{\rho_d} v_{max}^2$$

ρ_m and ρ_d are computed at the point of maximum 10m azimuthal wind speed v_{max}. ρ_m and ρ_d are the densities of humid and dry air:

$$\rho_m = \frac{p_d}{R_d T} + \frac{p_v}{R_v T},$$
$$\rho_d = \frac{p_d}{R_d T}.$$

Here, p_v (Pa) is the partial pressure of water vapor. p_v is defined as equal to e_p. ρ_d is equivalent to ρ but is denoted ρ_d in this Appendix for clarity.

The potential intensity, v_{pi} (m s^{-1}), is an upper bound on v_{max}. For each SST simulation, it is computed based on the time- and horizontal-mean vertical profiles of pressure, temperature, and water vapor mixing ratio from the last 20 days of the corresponding RCE simulation. For the calculation, we use an improved version of the Bister and Emanuel (2002) algorithm (Gilford 2020, 2021) assuming that $\frac{c_k}{c_d}$=0.9 and that any ascent was pseudoadiabatic. A kinetic energy per unit mass of dry air, $KE_{v_{pi}}$ is then defined based on v_{pi}. The calculation of $KE_{v_{pi}}$ is largely analogous to the definition of $KE_{v_{max}}$, except that we use interpolated values of ρ_d and ρ_m at 10m that are calculated based on domain-average values of ρ_m and ρ_d at the surface and at 25m in the RCE simulations. In contrast, ρ_m and ρ_d in the calculation of $KE_{v_{max}}$ are interpolated specifically to the point of the maximum 10m azimuthal wind in the axisymmetric simulations.

The surface precipitation rate (kg m^{-2} s^{-1}) is included in the output of CM1. Using this, we calculate the horizontal-mean, time-average surface precipitation rate in the subdomain for each 2-day period. The integrated kinetic energy (IKE) is defined as in Powell and Reinhold (2007), with the exception that the horizontal wind speed at 10m, rather than the total wind speed at 10m, is used because the former is an output of CM1 while the latter is not, and because the vertical wind speed should be much smaller than the horizontal wind speed at this level:

$$IKE = \int_V \frac{1}{2}\rho_m U^2 dV.$$

dV is the volume element centered on a height of 10m and has a thickness of 1 meter in the vertical direction. ρ_m is the density of humid air and U is the horizontal wind speed, both at a height of 10m.

The surface sensible (SHF), latent (LHF), and total heat fluxes (THF) (W m^{-2}) are defined using the bulk formulae from CM1:

$$SHF = \rho_m c_p c_k U(\theta_s - \theta_{25})$$
$$LHF = \rho_m L_v c_k U(r^*(T_s) - r_{25})$$
$$THF = SHF + LHF$$

Here, ρ_m is the density of humid air at the surface, U is the horizontal wind speed at 10m, and c_k is the enthalpy exchange coefficient. $r^*(T_s)$ (kg kg^{-1}) is the saturation water vapor mixing ratio at the surface (Bolton 1980), θ_s is the potential temperature (K) at the surface, and θ_{25} and r_{25} are the potential temperature and water vapor mixing ratio at the lowest model level: 25m. In the formula for the SHF, the absolute temperature difference is approximated by the potential temperature difference.

For this study, we examine the variability of the horizontal- and time-averages of all quantities except the IKE and $KE_{v_{max}}$ during the time period under consideration. For the IKE and $KE_{v_{max}}$, only the time-average value is computed.

APPENDIX C

Sensitivity of MAFALDA-derived variables to the reference entropy choice

When defining the entropy, we must choose its value in the reference state. This reference entropy can be defined fully by choosing the values of the specific entropies of dry air and liquid water in the reference state, $s_{d,0}$ and $s_{l,0}$. In our work, we use a definition of the moist entropy that assumes $s_{d,0}$ and $s_{l,0}$ are zero. However, other definitions of entropy have been used in the literature, including the absolute entropy of Marquet (2017). Any study using MAFALDA with a different definition of the entropy must account for the ways this impacts some of the MAFALDA-derived variables.

The MAFALDA-derived terms that would change under a different entropy definition are W_{Max}, ΔG, and W_{Moist}. W_{Max} is calculated as $\oint \tilde{T} d\tilde{s}$ for each MAFALDA trajectory. Because of this, it will be directly affected by a different definition of the reference entropy. By definition, the specific Gibbs free energy of water in each of its phases, w, is $g_w = h_w - T s_w$. From this, we can see that the specific Gibbs free energies of water in all its phases will be impacted by both the choice of the reference entropy and the choice of the reference enthalpy. Since ΔG depends on the specific Gibbs free energies of water, the value of ΔG will change if a different entropy definition is chosen. Since W_{Moist} is dependent on ΔG, this variable will also be impacted.

In what follows, X_{gen} will denote the value of a MAFALDA-derived variable when some general definition of the entropy is used. If a different definition of the entropy were to be used then, assuming $s_{l,0}$ and $s_{d,0}$ are constant, the MAFALDA terms discussed above would be modified as follows:

$$W_{Max,gen} = W_{Max} - s_{l,0} \oint \tilde{r}_t d\tilde{T}$$

$$\Delta G_{gen} = \Delta G - s_{l,0} \sum_{w=v,l,i} \oint \tilde{T} d\tilde{r}_w$$

$$W_{Moist,gen} = W_{Moist} - s_{l,0} \sum_{w=v,l,i} \oint \tilde{T} d\tilde{r}_w$$

Although the differential heating defined in section 2b is a function of entropy, it can be rewritten, using the Gibbs relationship, in such a way that it does not depend on entropy (Pauluis and Zhang 2017):

$$dq = T ds + \sum_{w=v,l,i} g_w dr_w = dh - \alpha_d dp$$

As such, the total heating, Q_{in}, will not be affected by changes in the entropy definition. As a result of this, the efficiencies considered in this work are also independent of the choice of reference entropy. However, both Q_{in} and the efficiencies do depend on the choice of reference enthalpy.

In MAFALDA, the mechanical work performed by the atmospheric flow, $W_P + W_{KE}$, is related both to the entropy transport via W_{Max}, and to the Gibbs penalty. The sensitivity of W_{Max} to the reference entropy reflects the fact that the choice of the reference state affects the entropy transport. However, it should be stressed here that the entropy transport captured by W_{Max} is not the total entropy transport, but represents only that associated with air motions. A second component of the atmospheric entropy transport is associated with the entropy transport by falling hydrometeors. When the atmospheric circulation transports water from the surface ocean to the colder atmosphere, falling rainfall carries the same amount of water back from the atmosphere to the ocean surface. The entropy transport associated with falling hydrometeors depends on the reference entropy as well - but this sensitivity cancels out with that of the entropy transport that contributes to W_{Max}.

There are two possible approaches in dealing with the entropy transport by falling hydrometeors. One option is to convert the MAFALDA cycles into closed cycles, by carrying condensed water on the descending part of the cycle, following the suggestion of Pauluis (2011). This has the advantage of making the cycles fully independent of the reference state, albeit at the expense of making the computation slightly more complicated. A second option, adopted here following the original formulation of MAFALDA, is to use liquid water as the reference state with the practical goal of minimizing the entropy transport by falling precipitation. Doing so ensures that the entropy transport by the air motions captured in W_{Max} is a good approximation of the total entropy transport. For other choices for the reference states - such as the absolute entropy of Marquet (2017) - falling precipitation carries a substantial amount of entropy that should be properly accounted for in the computation of thermodynamic cycles.

References

Berrisford, P., and Coauthors, 2011: The ERA-Interim Archive Version 2.0, ERA Report Series 1, ECMWF, Shinfield Park, Reading, UK. 13177, https://doi.org/10.1007/BF01030791.

Bister, M., and K. A. Emanuel, 1998: Dissipative heating and hurricane intensity. *Meteor. Atmos. Phys.*, **65**, 233–240, https://doi.org/10.1007/BF01030791.

Bister, M., and K. A. Emanuel, 2002: Low frequency variability of tropical cyclone potential intensity 1. Interannual to interdecadal variability. *J. Geophys. Res.*, **107**, 4801, https://doi.org/10.1029/2001JD000776.

Bister, M., N. Renno, O. Pauluis, and K. A. Emanuel, 2011: Comment on Makarieva et al. 'a critique of some modern applications of the Carnot heat engine concept: the dissipative heat engine cannot exist'. *Proc. R. Soc. A*, **467**, 1–6, https://doi.org/10.1098/rspa.2010.0087.

Bolton, D., 1980: The Computation of Equivalent Potential Temperature. *Mon. Wea. Rev.*, **108**, 1046–1053, https://doi.org/10.1175/1520-0493(1980)108⟨1046:TCOEPT⟩2.0.CO;2.

Bretherton, C. S., P. N. Blossey, and M. Khairoutdinov, 2005: An Energy-Balance Analysis of Deep Convective Self-Aggregation above Uniform SST,. *J. Atmos. Sci.*, **62**, 4273–4292, https://doi.org/10.1175/JAS3614.1.

Bryan, G. H., and J. M. Fritsch, 2002: A Benchmark Simulation for Moist Nonhydrostatic Numerical Models. *Mon. Wea. Rev.*, **130**, 2917–2928, https://doi.org/10.1175/1520-0493(2002)130⟨2917:ABSFMN⟩2.0.CO;2.

Bryan, G. H., and R. Rotunno, 2009: The Maximum Intensity of Tropical Cyclones in Axisymmetric Numerical Model Simulations. *Mon. Wea. Rev.*, **137**, 1770–1789, https://doi.org/10.1175/2008MWR2709.1.

Chemke, R., and L. M. Polvani, 2019: Opposite tropical circulation trends in climate models and in reanalyses. *Nat. Geosci.*, **12**, 528–532, https://doi.org/10.1038/s41561-019-0383-x.

Dee, D. P., and Coauthors, 2011: The ERA-Interim reanalysis: configuration and performance of the data assimilation system. *Q.J.R. Meteorol. Soc.*, **137**, 553–597, https://doi.org/10.1002/qj.828.

Defforge, C. L., and T. M. Merlis, 2017: Evaluating the Evidence of a Global Sea Surface Temperature Threshold for Tropical Cyclone Genesis. *J. Climate*, **30**, 9133–9145, https://doi.org/10.1175/JCLI-D-16-0737.1.

Dunion, J. P., 2011: Rewriting the Climatology of the Tropical North Atlantic and Caribbean Sea Atmosphere. *J. Climate*, **24**, 893–908, https://doi.org/10.1175/2010JCLI3496.1.

Emanuel, K. A., 1986: An Air-Sea Interaction Theory for Tropical Cyclones. part I: Steady-State Maintenance. *J. Atmos. Sci.*, **43**, 585–604, https://doi.org/10.1175/1520-0469(1986)043⟨0585:AASITF⟩2.0.CO;2.

Fang, J., O. Pauluis, and F. Zhang, 2019: The Thermodynamic Cycles and Associated Energetics of Hurricane Edouard (2014) during Its Intensification. *J. Atmos. Sci.*, **76**, 1769–1784, https://doi.org/10.1175/JAS-D-18-0221.1.

Gilford, D. M., 2020: Potential Intensity Calculations in Python, pyPI v1.3. Zenodo. https://doi.org/10.5281/zenodo.3985975.

Gilford, D. M., 2021: Tropical Cyclone Potential Intensity Calculations in Python. *Geosci. Model Dev.*, **14**, 2351–2369, https://doi.org/10.5194/gmd-14-2351-2021.

Goff, J. A., and S. Gratch, 1946: Low-pressure properties of water from -160 to 212 f, in Transactions of the American Society of Heating and Ventilating Engineers, presented at the 52nd annual meeting of the American Society of Heating and Ventilating Engineers. 95–122.

Golitsyn, G., 1970: A similarity approach to the general circulation of planetary atmospheres. *Icarus*, **13**, 1–24, https://doi.org/10.1016/0019-1035(70)90112-0.

Hakim, G. J., 2011: The Mean State of Axisymmetric Hurricanes in Statistical Equilibrium. *J. Atmos. Sci.*, **68**, 1364–1376, https://doi.org/10.1175/2010JAS3644.1.

Held, I. M., and B. J. Soden, 2006: Robust Responses of the Hydrological Cycle to Global Warming. *J. Climate*, **19**, 5686–5699, https://doi.org/10.1175/JCLI3990.1.

Holland, G. J., 1980: An Analytic Model of the Wind and Pressure Profiles in Hurricanes. *Mon. Wea. Rev.*, **108**, 1212–1218, https://doi.org/10.1175/1520-0493(1980)108⟨1212:AAMOTW⟩2.0.CO;2.

Hong, S.-Y., Y. Noh, and J. Dudhia, 2006: A New Vertical Diffusion Package with an Explicit Treatment of Entrainment Processes. *Mon. Wea. Rev.*, **134**, 2318–2341, https://doi.org/10.1175/MWR3199.1.

Jeevanjee, N., and D. M. Romps, 2018: Mean precipitation change from a deepening troposphere. *Proc. Natl. Acad. Sci. (USA)*, **115**, 11 465–11 470, https://doi.org/10.1073/pnas.1720683115.

Kalnay, E., and Coauthors, 1996: The NCEP/NCAR 40-Year Reanalysis Project. *Bull. Amer. Meteor. Soc.*, **77**, 437–472, https://doi.org/10.1175/1520-0477(1996)077⟨0437:TNYRP⟩2.0.CO;2.

Kanamitsu, M., W. Ebisuzaki, J. Woollen, S.-K. Yang, J. J. Hnilo, M. Fiorino, and G. L. Potter, 2002: NCEP–DOE AMIP-II Reanalysis (R-2). *Bull. Amer. Meteor. Soc.*, **83**, 1631–1644, https://doi.org/10.1175/BAMS-83-11-1631.

Khairoutdinov, M. F., and K. A. Emanuel, 2013: Rotating radiative-convective equilibrium simulated by a cloud-resolving model. *Journal of Advances in Modeling Earth Systems*, **5**, 816–825, https://doi.org/10.1002/2013MS000253.

Kistler, R., and Coauthors, 2001: The NCEP–NCAR 50-Year Reanalysis: Monthly Means CD-ROM and Documentation. *Bull. Amer. Meteor. Soc.*, **82**, 247–268, https://doi.org/10.1175/1520-0477(2001)082⟨0247:TNNYRM⟩2.3.CO;2.

Klotzbach, P. J., S. G. Bowen, J. R. Pielke, and M. Bell, 2018: Continental U.S. Hurricane Landfall Frequency and Associated Damage: Observations and Future Risks. *Bull. Amer. Meteor. Soc.*, **99**, 1359–1376, https://doi.org/10.1175/BAMS-D-17-0184.1.

Knietzsch, M.-A., A. Schröder, V. Lucarini, and F. Lunkeit, 2015: The impact of oceanic heat transport on the atmospheric circulation. *Earth Syst. Dynam.*, **6**, 591–615, https://doi.org/10.5194/esd-6-591-2015.

Knutson, T. R., and R. E. Tuleya, 2004: Impact of CO2-Induced Warming on Simulated Hurricane Intensity and Precipitation: Sensitivity to the Choice of Climate Model and Convective Parameterization. *J. Climate*, **17**, 3477–3495, https://doi.org/10.1175/1520-0442(2004)017⟨3477:IOCWOS⟩2.0.CO;2.

Kreussler, P., and Coauthors, 2021: Tropical cyclone integrated kinetic energy in an ensemble of HighResMIP simulations. *Geophys. Res. Lett.*, **48**, e2020GL090 963, https://doi.org/10.1029/2020GL090963.

LaLiberté, F., J. Zika, L. Mudryk, P. Kushner, J. Kjellsson, and K. Döös, 2015: Constrained work output of the moist atmospheric heat engine in a warming climate. *Science*, **347**, 540–543, https://doi.org/10.1126/science.1257103.

Lembo, V., F. Lunkeit, and V. Lucarini, 2019: TheDiaTo (v1.0) – a new diagnostic tool for water, energy and entropy budgets in climate models. *Geosci. Model Dev.*, **12**, 3805–3834, https://doi.org/10.5194/gmd-12-3805-2019.

Li, Y., Y. Wang, and Z.-M. Tan, 2023: Is the outflow-layer inertial stability crucial to the energy cycle and development of tropical cyclones? *J. Atmos. Sci.*, https://doi.org/10.1175/JAS-D-22-0186.1.

Lucarini, V., K. Fraedrich, and F. Lunkeit, 2010a: Thermodynamic analysis of snowball Earth hysteresis experiment: Efficiency, entropy production and irreversibility. *Q.J.R. Meteorol. Soc.*, **136**, 2–11, https://doi.org/10.1002/qj.543.

Lucarini, V., K. Fraedrich, and F. Lunkeit, 2010b: Thermodynamics of climate change: generalized sensitivities. *Atmos. Chem. Phys.*, **10**, 9729–9737, https://doi.org/10.5194/acp-10-9729-2010.

MacKinnon, J. G., and H. White, 1985: Some heteroskedasticity-consistent covariance matrix estimators with improved finite sample properties. *Journal of Econometrics*, **29**, 305–325, https://doi.org/10.1016/0304-4076(85)90158-7.

Marquet, P., 2017: A Third-Law Isentropic Analysis of a Simulated Hurricane. *J. Atmos. Sci.*, **74**, 3451–3471, https://doi.org/10.1175/JAS-D-17-0126.1.

Mrowiec, A. A., O. M. Pauluis, and F. Zhang, 2016: Isentropic Analysis of a Simulated Hurricane. *J. Atmos. Sci.*, **73**, 1857–1870, https://doi.org/10.1175/JAS-D-15-0063.1.

Ozawa, H., and S. Shimokawa, 2015: Thermodynamics of a tropical cyclone: generation and dissipation of mechanical energy in a self-driven convection system. *Tellus A: Dynamic Meteorology and Oceanography*, **67**, https://doi.org/10.3402/tellusa.v67.24216.

O'Neill, M., and D. R. Chavas, 2020: Inertial Waves in Axisymmetric Tropical Cyclones. *J. Atmos. Sci.*, **77**, 2501–2517, https://doi.org/10.1175/JAS-D-19-0330.1.

Pan, Y., L. Li, X. Jiang, G. Li, W. Zhang, X. Wang, and A. P. Ingersoll, 2017: Earth's changing global atmospheric energy cycle in response to climate change. *Nat. Commun.*, **8**, 14 367, https://doi.org/10.1038/ncomms14367.

Pauluis, O., V. Balaji, and I. M. Held, 2000: Frictional Dissipation in a Precipitating Atmosphere. *J. Atmos. Sci.*, **57**, 989–994, https://doi.org/10.1175/1520-0469(2000)057⟨0989:FDIAPA⟩2.0.CO;2.

Pauluis, O., and I. M. Held, 2002a: Entropy Budget of an Atmosphere in Radiative–Convective Equilibrium. Part I: Maximum Work and Frictional Dissipation. *J. Atmos. Sci.*, **59**, 125–139, https://doi.org/10.1175/1520-0469(2002)059⟨0125:EBOAAI⟩2.0.CO;2.

Pauluis, O., and I. M. Held, 2002b: Entropy Budget of an Atmosphere in Radiative–Convective Equilibrium. Part II: Latent Heat Transport and Moist Processes. *J. Atmos. Sci.*, **59**, 140–149, https://doi.org/10.1175/1520-0469(2002)059⟨0140:EBOAAI⟩2.0.CO;2.

Pauluis, O. M., 2011: Water Vapor and Mechanical Work: A Comparison of Carnot and Steam Cycles. *J. Atmos. Sci.*, **68**, 91–102, https://doi.org/10.1175/2010JAS3530.1.

Pauluis, O. M., 2016: The Mean Air Flow as Lagrangian Dynamics Approximation and Its Application to Moist Convection. *J. Atmos. Sci.*, **73**, 4407–4425, https://doi.org/10.1175/JAS-D-15-0284.1.

Pauluis, O. M., and A. A. Mrowiec, 2013: Isentropic Analysis of Convective Motions. *J. Atmos. Sci.*, **70**, 3673–3688, https://doi.org/10.1175/JAS-D-12-0205.1.

Pauluis, O. M., and F. Zhang, 2017: Reconstruction of Thermodynamic Cycles in a High-Resolution Simulation of a Hurricane. *J. Atmos. Sci.*, **74**, 3367–3381, https://doi.org/10.1175/JAS-D-16-0353.1.

Powell, M. D., and T. A. Reinhold, 2007: Tropical Cyclone Destructive Potential by Integrated Kinetic Energy. *Bull. Amer. Meteor. Soc.*, **88**, 513–526, https://doi.org/10.1175/BAMS-88-4-513.

Romps, D. M., 2008: The Dry-Entropy Budget of a Moist Atmosphere. *J. Atmos. Sci.*, **65**, 3779–3799, https://doi.org/10.1175/2008JAS2679.1.

Singh, M. S., and P. A. O'Gorman, 2016: Scaling of the entropy budget with surface temperature in radiative-convective equilibrium. *Journal of Advances in Modeling Earth Systems*, **8**, 1132–1150, https://doi.org/10.1002/2016MS000673.

Singh, M. S., and M. E. O'Neill, 2022: The climate system and the second law of thermodynamics. *Rev. Mod. Phys.*, **94**, 015 001, https://doi.org/10.1103/RevModPhys.94.015001.

Thorne, P. W., and R. S. Vose, 2010: Reanalyses Suitable for Characterizing Long-Term Trends. *Bull. Amer. Meteor. Soc.*, **91**, 353–362, https://doi.org/10.1175/2009BAMS2858.1.

Trenberth, K. E., A. Dai, R. M. Rasmussen, and D. B. Parsons, 2003: The Changing Character of Precipitation. *Bull. Amer. Meteor. Soc.*, **84**, 1205–1218, https://doi.org/10.1175/BAMS-84-9-1205.

Uppala, S. M., and Coauthors, 2005: The ERA-40 re-analysis. *Q.J.R. Meteorol. Soc.*, **131**, 2961–3012, https://doi.org/10.1256/qj.04.176.

Wang, D., and Y. Lin, 2021: Potential Role of Irreversible Moist Processes in Modulating Tropical Cyclone Surface Wind Structure. *J. Atmos. Sci.*, **78**, 709–725, https://doi.org/10.1175/JAS-D-20-0192.1.

Wang, S., and R. Toumi, 2021: Recent tropical cyclone changes inferred from ocean surface temperature cold wakes. *Scientific Reports*, **11**, 22 269, https://doi.org/10.1038/s41598-021-01612-9.

Wilhelmson, R. B., and C.-S. Chen, 1982: A Simulation of the Development of Successive Cells Along a Cold Outflow Boundary. *J. Atmos. Sci.*, **39**, 1466–1483, https://doi.org/10.1175/1520-0469(1982)039⟨1466:ASOTDO⟩2.0.CO;2.

Zhang, Q., L. Wu, and Q. Liu, 2009: Tropical Cyclone Damages in China 1983–2006. *Bull. Amer. Meteor. Soc.*, **90**, 489–496, https://doi.org/10.1175/2008BAMS2631.1.